Article

Investigation of a Dual-Layer Metasurface-Inspired Fractal Antenna with Dual-Polarized/-Modes for 4G/5G Applications

Asutosh Mohanty [1], Bikash Ranjan Behera [2], Karu P. Esselle [3], Mohammed H. Alsharif [4,*], Abu Jahid [5,*] and Syed Agha Hassnain Mohsan [6]

1 School of Electronics Engineering, Kalinga Institute of Industrial Technology Bhubaneswar, Odisha 751024, India; asutoshmohanty.kiit0409@gmail.com
2 Department of Electronics and Communication Engineering, Centre for Advanced Post Graduate Studies (BPUT) Rourkela, Odisha 769015, India; bikashranjan.behera@gmail.com
3 School of Electrical and Data Engineering, University of Technology Sydney, Sydney, NSW 2109, Australia; Karu.Esselle@uts.edu.au
4 Department of Electrical Engineering, College of Electronics and Information Engineering, Sejong University, Seoul 05006, Korea
5 School of Electrical Engineering and Computer Science, University of Ottawa, 25 Templeton St., Ottawa, ON K1N 6N5, Canada
6 Ocean College, Zhejiang University, Zheda Road 1, Zhoushan 316021, China; hassnainagha@zju.edu.cn
* Correspondence: malsharif@sejong.ac.kr (M.H.A.); ajahi011@uottawa.ca (A.J.)

Abstract: In this research article, a dual-polarized compact bow-tie-shaped irregular fractal antenna with a dual metasurface (DMS) for directional radiation applications is designed using a dual-mode simple feeding mechanism. A short-circuited strip linked between the impedance transformation feed and the radiating patch activates the induced coupling modes, which are capacitive (C-mode) and inductive (L-mode), respectively. The C-mode antenna operates at 2.39–2.53 GHz, whereas the L-mode antenna operates at 2.88–4.49 GHz. It comprises a DMS positioned at $0.22\lambda_\circ$ from the antenna with $0.016\lambda_\circ$ separation and a 4×4 array of checkerboard type hole-injected tiny unit cells on each metasurface. A rectangular cavity-backed slot was employed as the ground plane to emulsify the reflected energy waves from the DMS, in order to start the coupling process with the boresight radiation, resulting in high gain and suppressed backward radiations. The gain in C-mode was 6.74 dBi, and the gain in L-mode was 7.7 dBi. For validation, a miniaturized metasurface antenna with the overall size of $0.32\lambda_\circ \times 0.32\lambda_\circ \times 0.22\lambda_\circ$ (where $\lambda_\circ$ is the free-space wavelength at 2.45 GHz) was fabricated and measured. The measured outcomes highlight its potential for 4G/5G wireless applications.

Keywords: bow-tie fractal radiator; coupling modes; dual-mode feed; dual-polarized patch; dual-metasurfaces (DMS)

1. Introduction

The rapid progress in wireless communication systems has emerged towards the evolution of hybrid wireless networks (LTE/3G/4G/5G). These hybrid networks form analog and digital topology, which demands larger bandwidth, high antenna gain, and enhanced system capacity for efficient signal coverage in smaller base stations. To meet such indispensable cellular protocols, antennas with multi-polarization are preferred owing to signal diversity. For such system requirements, highly compact antenna systems would be effective in a premium space. Moreover, incorporating reflectors for gain enhancement, radiation stability, and bandwidth is another challenge. Hence, deficiencies in perfect electric conductor (PEC) reflectors are compensated by introducing the artificial magnetic conductor (AMC) reflectors or metasurface (MS) reflectors due to their efficient electromagnetic (EM) waves reflection properties to optimize antenna bandwidth, gain, and radiation response for the proposed antenna [1–3].

In [4], a monopole-based dual-band antenna engineered on complementary split-ring resonators MS with a compact footprint of $0.062\lambda^5_{1.9GHz}$ and average gain of 4.3 dBi was discussed. The MS was employed as a decoupling method in [5] for closely packed dual-band antennas for MIMO applications, with the size of $1.11\lambda^2_{2.6GHz}$ and an average gain of 8.2 dBi. Using MS and meta superstate as a decoupling design, LP antennas in [6] were coupled to E-plane and H-plane for 5G base stations with the size of $1.21\lambda^2_{3.3GHz}$ and an average gain of 7 ± 0.2 dBi. In [7], the non-uniform MS was deployed for broadband dual-polarized antenna for base stations with a size of $0.54\lambda^2_{0.96GHz}$ and average gain of 7.4–9.2 dBi. A wideband printed antenna based upon the $\lambda/2$ cavity was introduced in [8] with size of $0.225\lambda^2_{2.3GHz}$ and average gain of 4.7 dBi.

On the other hand, AMC reflectors often provide excellent uni-directional radiation properties and a low-profile structure in comparison with respect to the PEC reflectors. In [9], a wideband MIMO antenna with profile height of $0.105\lambda_{3GHz}$, realized on an AMC reflector, was designed to obtain the average gain of 7.1 dBi with the antenna size of $0.75\lambda^2_{3GHz}$. A dual-polarized wideband LP antenna with the AMC profile height of $0.27\lambda_{2.7GHz}$ was achieved in [10], which was $3.24\lambda^2_{2.7GHz}$ and had a gain of 6.3 dBi. To achieve miniaturization, a $0.011\lambda^2_{2.9GHz}$ printed slot antenna that exhibits a magnetic, complementary capacitively loaded loop (CCLL) loaded MTM was designed in [11], with realized gain of 4 dBi. In [12], a CP diversity antenna using large-sized AMC reflectors with a profile height of $0.12\lambda_{4.5GHz}$ and gain of 6 dBi was designed for broadband applications. The crossed dipole radiation arms had a size of $0.24\lambda_{1.45GHz}$. A bow-tie-shaped antenna [13] structured on a plum-shaped AMC reflector with a profile height of $0.101\lambda_{3.21GHz}$ and gain of 9.7 dBi with an antenna size of $1.63\lambda^2_{3.21\,GHz}$ has been proposed for LTE applications. A fractal-shaped AMC reflector with a profile height of $0.124\lambda_{1.7GHz}$ was designed in [14] below a bow-tie-shaped dipole antenna of $0.112\lambda^2_{1.7\,GHz}$ with a gain of 6.5 dBi.

Since modern wireless communication applications need a compact integrated antenna system. Thus, reduced antenna size and good performance are considered to be the essential combined metrics. Self-similar structures are also alternative solutions, in terms of compactness and compromise design deficiencies. In the aforementioned reported literature, antenna size with profile compactness seems to be challenging for premium space utilization. Although some literature has good antenna performances, on the other hand, antenna size seems to be a major challenge. Hence, to alleviate the above issues, the antenna, along with the reflector size, has been reduced, and its performance metrics were optimized and enhanced. In this literature, a dual-mode induced dual-polarized compact directional antenna was realized with the dual AMC-MS layers. A number of similar instances in [15–21] were reported, but the proposed design achieved size reduction both in antenna ($0.0256\lambda_\circ$) and in MS constitutive units ($0.102\lambda_\circ$). The spacing in between the AMC-MS layers was only $0.016\lambda_\circ$, and the profile height was $0.22\lambda_\circ$ (i.e., 27.2 mm nearly equal to the quarter-wavelength). By employing dual AMC-MS, gain at dual-modes was increased >3 dBi compared to conventional operating modes. The cavity-backed slot ground emulsified the radiated waves to increase boresight gain and cross-pol. There was a reduction in its radiation planes, suitable from the application point of view.

2. Antenna Configuration

The proposed antenna configuration is presented in Figure 1. Figure 1a highlights the top view of a bow-tie-shaped fractal radiator antenna invoked with the dual-mode coupled feed. The antenna was fabricated on substrate 1 (FR-4, h_1 = 1.6 mm, ϵ_r = 4.3, and $\tan\delta$ = 0.02) of size $L_s \times L_s$. The cavity-backed slot ground plane (Ground 1) of the perimeter $2 \times (L_g + L_z)$ is shown in Figure 1b. Figure 1c shows the top-view of AMC-MS reflector of size $W_{MS} \times W_{MS}$, comprised of a 4 × 4 array of checkerboard-hole-injected unit cells nested in a squared metallic boundary of thickness W_M. Figure 1d illustrates the side view of the proposed antenna configuration, which is loaded with the dual AMC-MS layers. The antenna is separated from AMC-MS surface 1; height: H_1. AMC-MS surface 1 separates AMC-MS surface 2; height: H_2. Each AMC-MS structure is fabricated on the FR-4 substrate

(substrate 2 and substrate 3) of thickness h_2, h_3 backed with the full ground planes (ground 2, ground 3). Table 1 gives the information about the dimensions of the proposed antenna configuration (i.e., including radiator + AMC-MS layers).
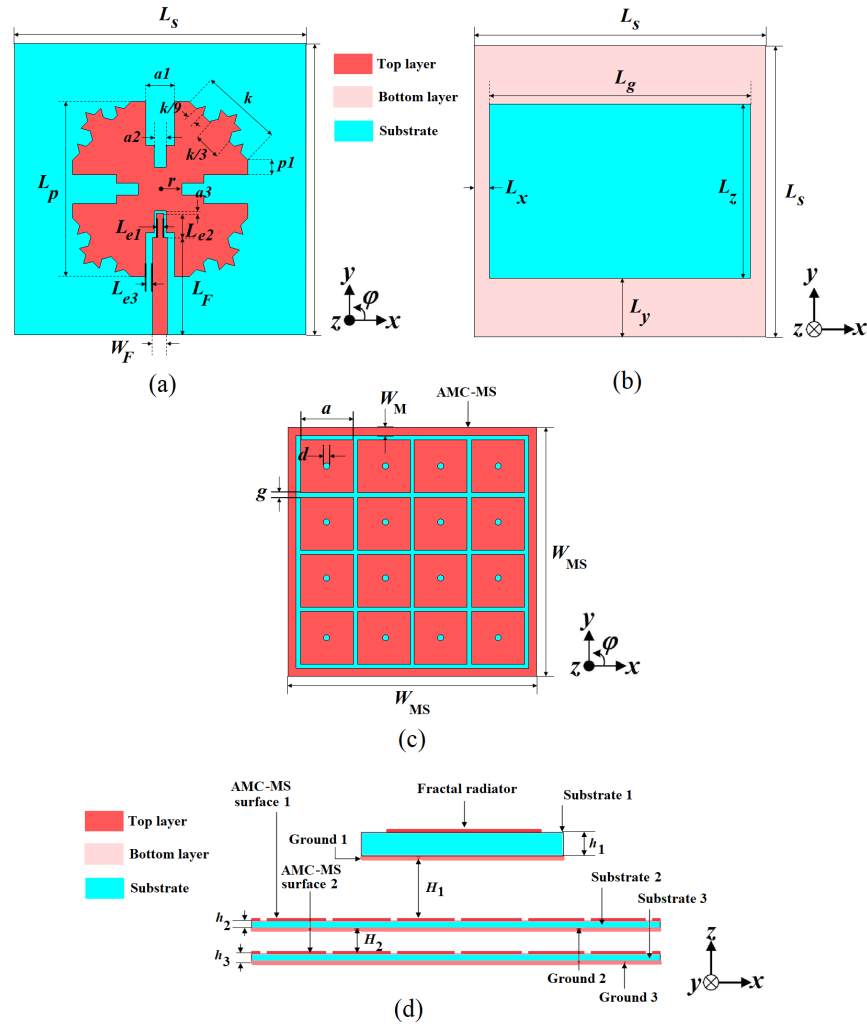

Figure 1. (**a**) Top view and (**b**) bottom view of the antenna; (**c**) top view of the AMC-MS reflector; and (**d**) side view of the antenna.

Table 1. Dimensions of the proposed antenna configuration (unit: All are in mm).

Parameter	Value	Parameter	Value	Parameter	Value
L_s	20	L_p	12	L_F	6.7
L_{e1}	0.5	L_{e2}	1.75	L_{e3}	0.5
W_F	1	a_1	2	a_2	0.8
p_1	1	k	5.65	r	1.5
L_x	1	L_y	4	L_z	12
L_g	18	h_1	1.6	h_2	1.6
h_3	1.6	H_1	27.2	H_2	2
a	8.5	d	1	g	0.7
W_m	1.3	W_{ms}	40	L_{unit1}	35
L_{unit2}	28.4	C_{unit}	2	g_{unit}	1.3
t_s	2	t_{cell}	1.6		

3. Antenna Design and Its Analysis

3.1. Dual-Mode Coupling Behaviour

The proposed antenna operates in two coupling modes, i.e., L-mode and C-mode, as shown in Figure 2. An impedance transition feed with a short-circuited strip behaves like an inductor (L-mode), and open-circuiting acts like a capacitor (C-mode). The coupling action of the feed and bow-tie radiating fractal patch antenna exhibits induced resonance coupling behavior and operates in distinct modes. A simplified circuit model was developed to illustrate the insights of the mode coupling mechanism. The feed represents an inductance, L_{feed}, which couples via the short-circuited strip, L_{strip} into the antenna surface impedance parameters consisting of L_{ant} and C_{ant}. From Figure 2a, the L-mode equivalent impedance, Z_L and resonant frequency, f_L, are expressed as:

$$Z_L = j\omega L_{feed} + j\omega L_{strip} + j\omega L_{ant} + \frac{1}{j\omega C_{ant}} \tag{1}$$

$$f_L = \frac{1}{2\pi\sqrt{\left(L_{feed} + L_{strip} + L_{ant}\right)C_{ant}}} \tag{2}$$

Similarly, a capacitance, C_c, is introduced via L_{feed} and L_{ant}, C_{ant} to effectively couple antenna in C-mode. Hence, from Figure 2b, the C-mode equivalent impedance, Z_c and resonant frequency, f_c can be expressed as:

$$Z_c = j\omega L_{feed} + \frac{1}{j\omega C_c} + j\omega L_{ant} + \frac{1}{j\omega C_{ant}} \tag{3}$$

$$f_c = \frac{1}{2\pi\sqrt{L_{feed}\left(\frac{C_c C_{ant}}{C_c + C_{ant}}\right)}} \tag{4}$$

The two coupling modes can be further explained by simulated electric field streamlines. Figure 3A,B illustrates the electric field streamlines of two coupling modes. In the case of C-mode, the current at point-A are divergent due to the isolation of the feed and radiator. The isolated region has an effective stored electric field which is equivalent to the capacitance between feed and radiator. During excitation, it usually forms an equipotential region due to the induced effect. So, the field's current streamlines are not condensed. But in the case of L-mode, the current at point-B are convergent due to the short-circuited strip between feed and radiator, and an inductive effect is generated. During the excitation, it forms a non-equipotential region due to the effect of magnetic fields that converge the currents to be condensed. So, dual mode effects are observed in the radiating surface, reported here.
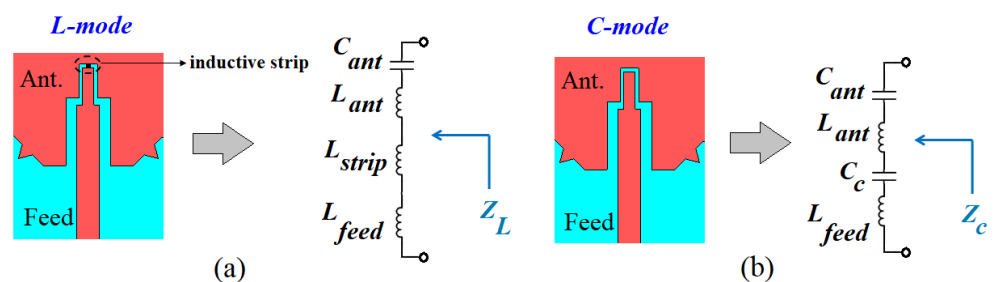

Figure 2. Dual coupling modes (operating modes) of the proposed antenna configuration: (**a**) L-mode and (**b**) C-mode.
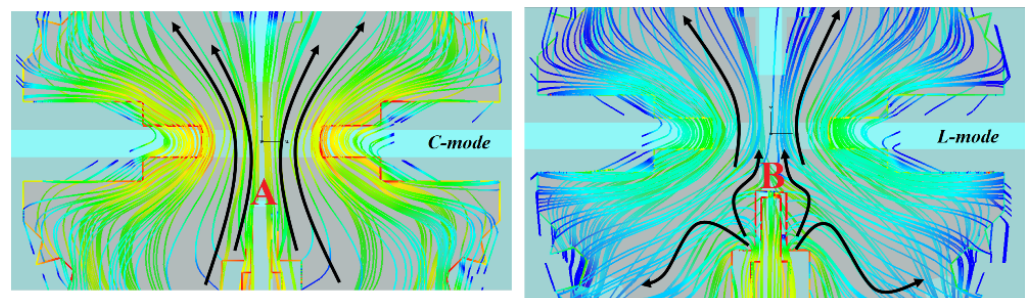
Figure 3. Simulated electric-field streamlines in C-mode and L-mode.

3.2. AMC-MS Unit Cell Analysis and Its Circuit Conception

To investigate the proposed AMC-MS shown in Figure 4a,b, the unit cell structure was initially investigated and analyzed in the periodic structure template of CST MWS studio suite unit cell workflow in a frequency domain solver. Here, the unit cell consists of a checkerboard-hole-injected with a squared loop boundary at the top and a metallic ground bottom sandwiched with an FR-4 substrate, t_{cell} = 1.6 mm, ϵ_r = 4.3, and tan δ = 0.02. Then, floquent boundary conditions are usually set into the unit cell with Z_{max} and Z_{min} as reference port terminals to obtain the reflection coefficient, dB and reflection phase (degree) shown in Figure 4d.
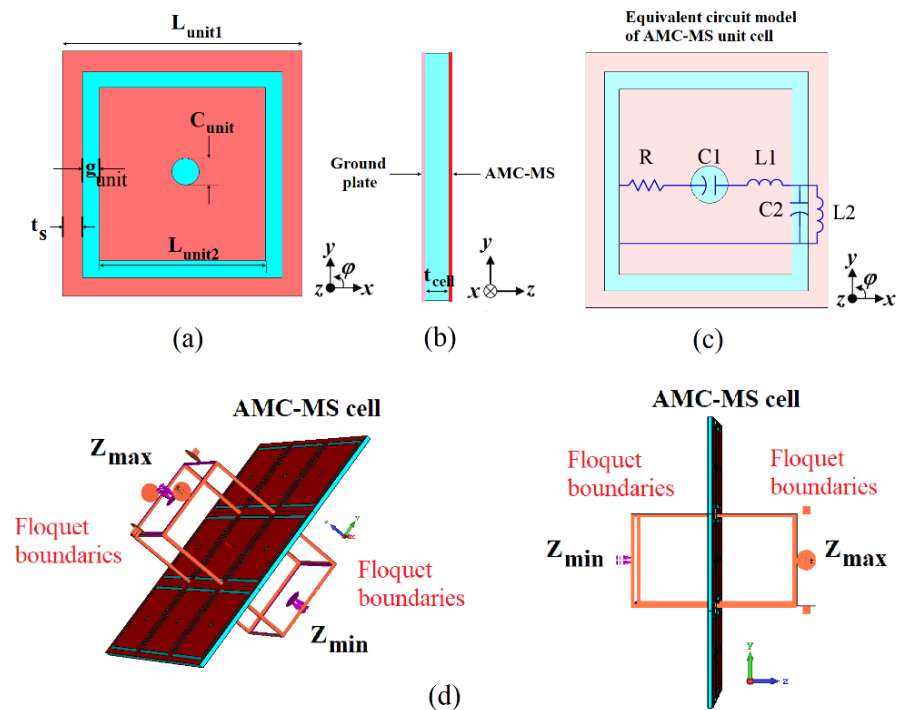

Figure 4. (**a**) Checkerboard-hole-injected unit cell: top view, (**b**) side view; (**c**) equivalent circuit model; and (**d**) floquent boundary arrangement of the unit cell with excitation ports Z_{max} and Z_{min}.

The AMC-MS unit cell had a sharp reflection S11, of magnitude −22.5 dB at 2.45 GHz, and the transmission parameter S12 almost converges to 0 dB at the same frequency, as shown in Figure 5a. Similarly, Figure 5b has an AMC-MS reflection phase at 2.45 GHz with the 0° reflection phase characteristic, in which all the unit cell structures are analyzed. In Figure 5c, the permittivity and permeability characteristics are shown. Here, the (AMC-MS-A, AMC-MS-B) unit-cell structures have some insignificant 0° phase reflection crossovers, and the proposed AMC-MS structure validates the design of our criteria. It is to be noted that the length L_{unit2} and the distance g_{unit} can modulate the AMC 0° phase crossover points to higher/lower frequencies. The equivalent circuit conception of the

proposed AMC-MS unit cell is shown in Figure 4c. As the circuit modeling includes cascading lumped elements, the L_{unit2} represents a series R-L1-C1 unit. The outer square loop metallic boundary represents an inductance L2, whereas the gap g_{unit} between L_{unit2} and t_s denotes a capacitance C2. Figure 6a shows the unit cell reflection magnitude for EM and circuit simulations, and Figure 6b gives an idea (insights) about the real and imaginary components for the same configuration.
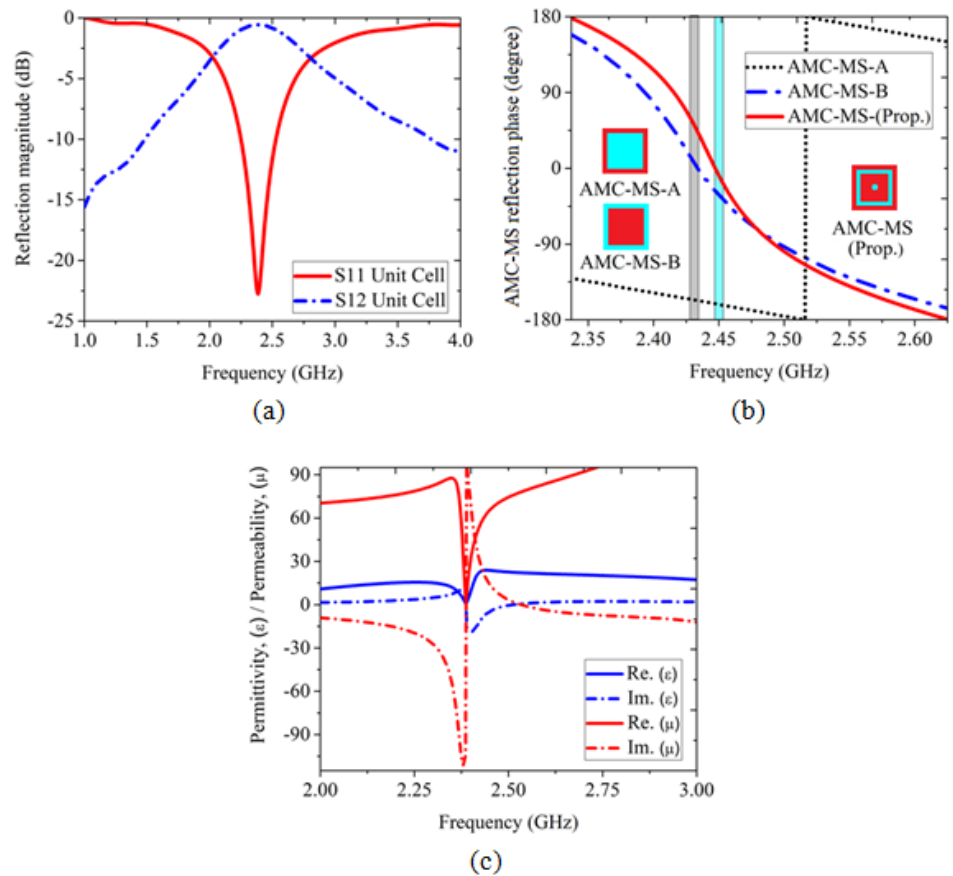

Figure 5. AMC-MS unit cell performance: (**a**) Reflection magnitude, (**b**) phase, and (**c**) permittivity (ε) and permeability (μ).
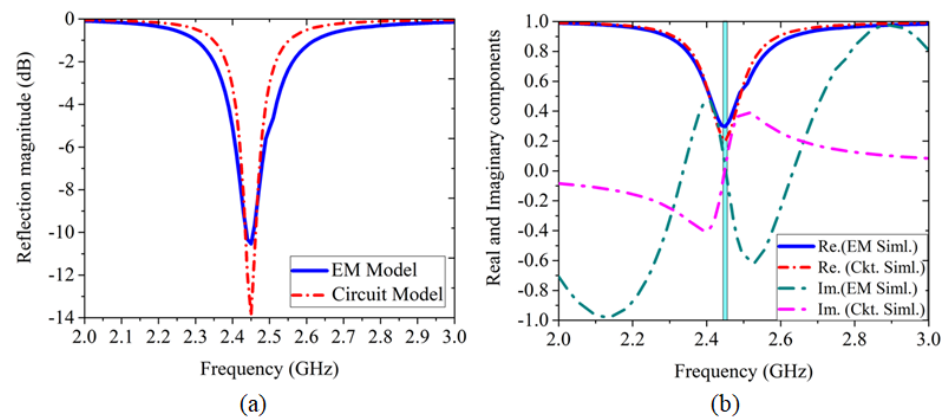

Figure 6. The simulated EM model and circuit model of AMC-MS unit cell: (**a**) Reflection magnitude, dB and (**b**) real & imaginary components. The equivalent circuit model parameters of the proposed unit cell are given by: R = 75 Ω, C1 = 0.02255 pF, L1 = 187.31 nH, C2 = 0.2 pF, L2 = 0.05 nH.

3.3. AMC-MS Equivalent Circuit Model

A simplified equivalent circuit model is shown in Figure 7 for the proposed AMC-MS structure [22]. The outer patch length (L_{unit1}) and inner patch length (L_{unit2}) provide inductance (L_a) and (L_u). The periodic gap (g_{unit}) between the successive array of unit cells corresponds to a capacitance (C_a). Since the unit cells in the periodic array are adjacent to each other, they can be viewed as a series of LC-lumped elements. Thus, the air gap between the AMC-MS1 and AMC-MS2 provides an inductance (L_h). Thus, the resulting inductance (L_h) is in parallel to the infinite series stacked array of periodic unit cells consisting of inductances and capacitance (L_a, C_a, L_u). Thus, the equivalent AMC-MS impedance can be expressed as ($\eta_{eq} = Z_x || Z_y$). The resulting impedance (η_{eq}) and resonant frequency (f_{eq}) of AMC-MS can be calculated as [23,24]:

$$\eta_{eq} = \frac{Z_x Z_y}{Z_x + Z_y} = \frac{j\omega L_h(1 - \omega^2 L_a C_a - \omega^2 L_u C_a)}{1 - \omega^2 L_a C_a - \omega^2 L_u C_a - \omega^2 L_h C_a} \tag{5}$$

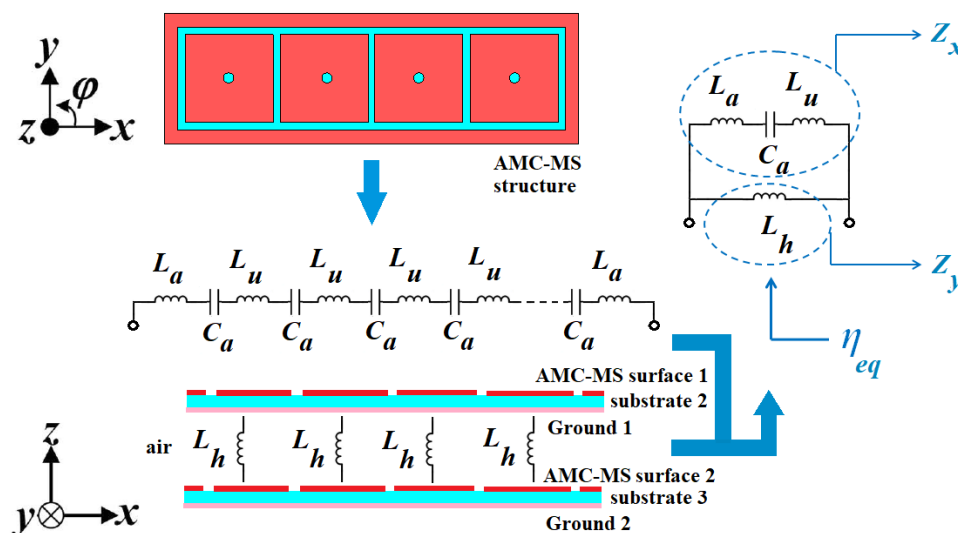$$f_{eq} = \frac{1}{2\pi\sqrt{(L_a + L_u + L_h)C_a}} \tag{6}$$

Figure 7. Equivalent circuit model of the proposed AMC-MS unit cell.

3.4. Dual-Polarized Bow-Tie Fractal Radiator

The duality behavior of bow-tie-shaped fractal radiator is primarily investigated through the surface current distribution (A/m) shown in Figure 8, for two-operating modes. In Figure 8a, for the C-mode at 2.45 GHz, surface currents are in distributed from $-y$ to $+y$. As the radiator has a bow-tie-shaped configuration, the diagonal currents are aligned in the same direction—i.e., currents at (1, 3) positions and (2, 4) are uni-directional. However, currents at (1, 2) positions and (3, 4) are axially symmetrical; thus, the antenna configurations assist centro-cyclic symmetry of the current distribution (considering the surface currents in the ground plane). Similarly, for the L-mode at 4.0 GHz, surface currents are distributed from $+y$ to $-y$, as shown in Figure 8b. As stated above, similar centro-cyclic surface current traces can be observed. If carefully noticed, from both surface currents' behavior, the antenna shows a symmetry of dual current trails. Henceforth, some important observations are highlighted that showcase the duality behavior of the proposed antenna as follows:

- The surface currents observed in a C-mode and L-mode are centro-symmetric in the bow-tie-shaped fractal radiator. Due to centro-symmetry, the length of current modes is $\lambda_\circ/2$, as shown in Figure 8.

- The duality modes can be further examined through 3D far-field E-pattern fields
(V), as shown in Figure 9. The E-field radiations in both modes almost exhibit equal
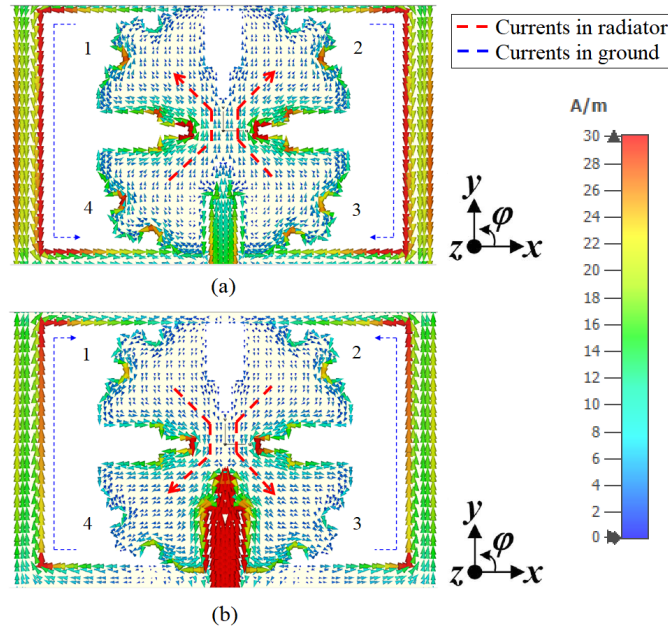magnitudes (V).

Figure 8. Surface current distributions on bow-tie shaped fractal radiator at (**a**) 2.45 GHz, (C-mode)
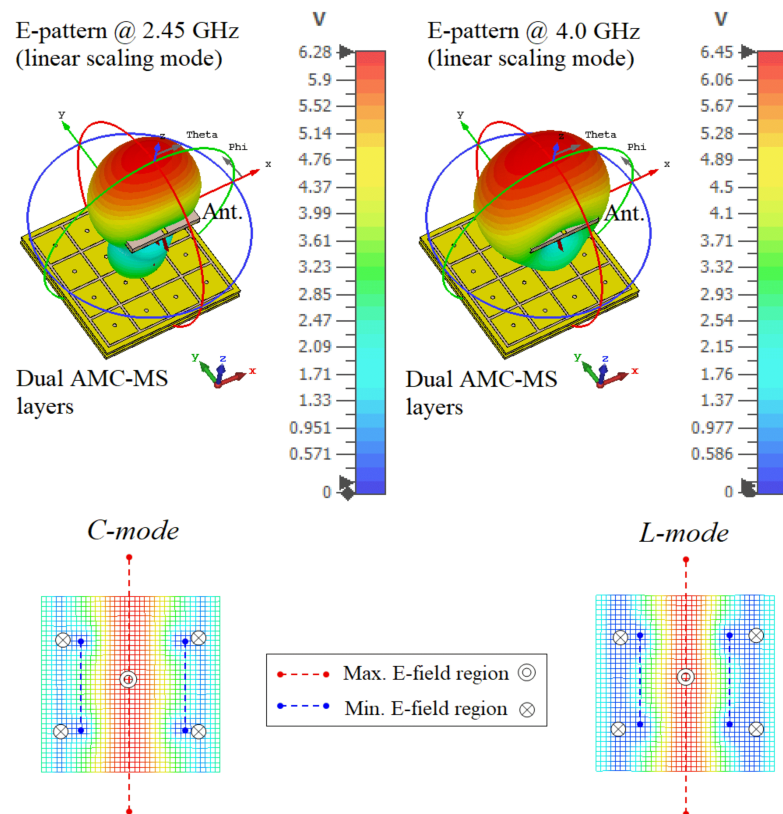and (**b**) 4.0 GHz, (L-mode).

Figure 9. 3D Radiation patterns and magnitude of radiated E-field intensity for C-mode at 2.45 GHz
and L-mode at 4.0 GHz.

- Generally, the radiation magnitude in the E-field at 2.45 GHz, C-mode has a maximum E-field region at the center (⊚) and minimum E-field region at the sides (⊗). The same effects are observed at 4.0 GHz for L-mode. So, the similar effects in radiation magnitude constricted due to dominant E-fields at dual bands are distinctively analogous to the 3D patterns.

3.5. Dual AMC-MS Layer Effects

It was found that a dual AMC-MS layered structure has the advantages of improving the antenna parameters such as S11, boresight radiation pattern, gain, and suppressed backward radiation [25,26]. Thus, the insights of AMC-MS with respect to reported work are summarized as follows:

- In Figure 10a, for C-mode, the impedance matching characteristics are shown for both with and without AMC-MS cases. Due to the effects of dual-loaded AMC-MS layers, the center frequencies are shifted to the lower bands. It can be seen that matching characteristics have been improved by >25 dBi at 2.45 GHz, with the dual AMC-MS. Similarly, impedance improvement effects with wideband can be observed for L-mode at 4.0 GHz in Figure 10b, with dual AMC-MS. Thus, the improvements in impedance matching in both modes are due to the effective coupling process, where the radiation and reflection waves are sufficiently coupled between the antenna and AMC-MS.
- The radiation pattern is generally bi-directional at $\theta = 0°$ (+ *z*-axis) and 180° (− *z*-axis) with no MS. To achieve, broadside radiation, MS was adopted (single AMC-MS) for maximum radiation at $\theta = 0°$ (+ *z*-axis), as shown in Figure 11a. However, the backward radiation is below −5 dBi, which is not suitable for good radiation stability in wireless applications. Thus, another AMC-MS was introduced (dual AMC-MS) to reduce the back radiation and enhance boresight radiation, providing a better front-to-back ratio (FBR) of −18 to −20 dBi.
- Without MS, the antenna witnessed a gain < 3 dBi. When a single AMC-MS is adopted, the gain is improved by 3 dBi. Then, the antenna gain is further improved by 3.3 dBi when the dual AMC-MS layers are implemented, as shown in Figure 11b and Table 2. To understand the impact of "H1", a parametric study is shown in Figure 12.
- The boresight gain at $\theta = 0°$ (+ *z*-axis) shows an improvement in radiation performance with dual AMC-MS layers. The 3D radiation pattern at the centered frequencies for two operating modes is shown in Figure 11c. Then, the C-mode and L-mode antenna configurations' performance summaries are presented in Table 2. Furthermore, the back lobe radiation characteristics at the corresponding modes are depicted in Table 3.
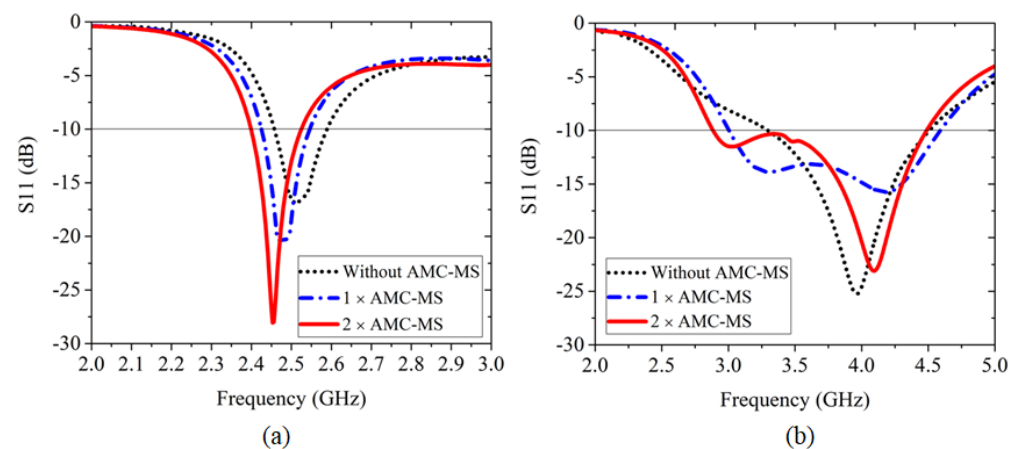

Figure 10. Comparison of S-parameters (S11, dB) without/with the presence of AMC-MS structures (layers) in the proposed antenna configuration for: (**a**) C-mode and (**b**) L-mode.
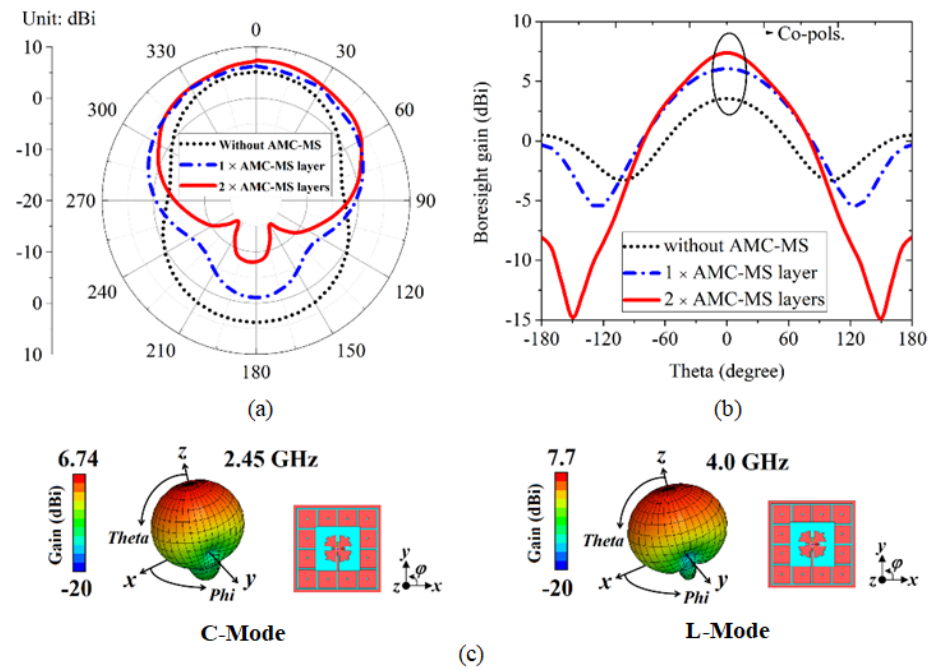
Figure 11. Comparison of far-field pattern without/with AMC-MS structures (layers) in the proposed antenna configuration for: (**a**) radiation pattern, (**b**) boresight gain without/with AMC-MS structures (layers), and (**c**) 3D radiation pattern at 2.45 GHz and 4.0 GHz.
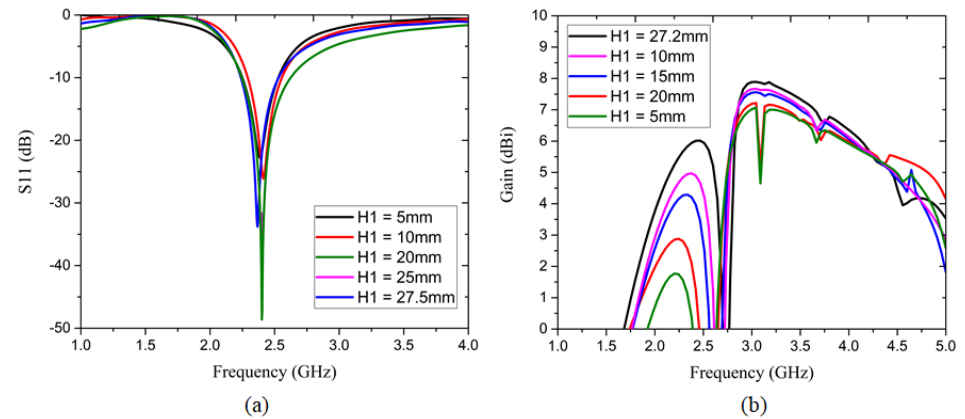

Figure 12. Parametric study showing the variation of "H1" on (**a**) S11, dB and (**b**) Gain, dBi.

Table 2. Comparison analysis of antenna working modes without/with the presence of AMC-MS structures (layers).

Antenna Configurations	C-Mode, Freq.	C-Mode, Gain	L-Mode, Freq.	L-Mode, Gain
No AMC-MS	2.46–2.59 GHz	2.8 dBi	3.26–4.5 GHz	3.0 dBi
1 × AMC-MS	2.42–2.75 GHz	>3.0 dBi	3–4.25 GHz	>5.0 dBi
2 × AMC-MS	**2.39–2.53 GHz**	**>6.0 dBi**	**2.88–4.49 GHz**	**>7.0 dBi**

Table 3. Back lobe radiation characteristics without/with the presence of AMC-MS structures (layers).

Antenna Configurations	C-Mode	L-Mode
No AMC-MS	−10 dBi	−10 dBi
1 × AMC-MS	−15 dBi	−15 dBi
2 × AMC-MS	**−20 dBi**	**−20 dBi**

3.6. Simulated Field Current Distributions

The simulated field current distributions with respect to the presence of dual AMC-MS layers on the radiator are analyzed, showing some distinctive radiation properties, as follows:

- In Figure 13a, the field's current lines are uncopulated. The isolated loop formation of currents provides weaker coupling energy; hence, all near-field radiated waves do not participate in the coupling process.
- Figure 13b shows that the field lines have symmetrically copulated when the AMC-MS layer is introduced, as a result of which, the near-field radiated waves participate in the coupling process due to in-phase field components of the AMC-MS reflector and contribute to higher radiation energy in the + z-axis. The presence of DMS combines the reflective field energy to effectively couple in the cavity-backed ground aperture, so boresight radiation energy is improved.
- The parabolic field lines form a stronger in-phase coupling process at the ground aperture and bow-tie-shaped patch radiator. Hence, radiative fields becomes additive in nature and enhance the radiation process in the boresight direction, $\theta = 0°$ (+ z-axis).
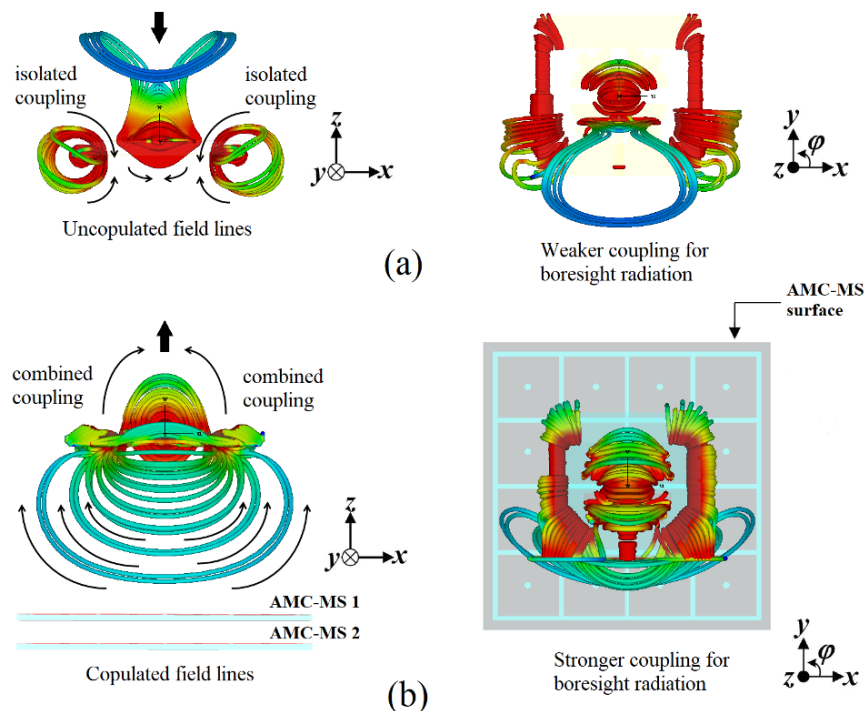

Figure 13. Surface current distributions of proposed antenna configuration: (**a**) without AMC-MS reflector and (**b**) with AMC-MS reflector.

4. Evaluation of Simulated and Measured Performance

To validate the proposed antenna, a prototype was fabricated and is shown in Figure 14. The S11 parameter was measured by the PNA series Microwave Network Analyzer (Model: N5222A) from Agilent technologies, and its radiation pattern was measured in a far-field anechoic chamber. Figure 15a,b shows the S11 plots for two operating modes. For C-mode, the simulated S11 ranged from 2.39 to 2.53 GHz, a bandwidth of 0.14 GHz, whereas the measured response had an S11 of 2.33–2.57 GHz, a bandwidth of 0.24 GHz. For L-mode, the simulated S11 ranged from 2.88 to 4.49 GHz, a bandwidth of 2.21 GHz, whereas the measured response had S11 of 2.91–4.53 GHz, a bandwidth of 1.62 GHz. Due to the inductance effect, sharp resonance was observed at 3.1 GHz. However, the measured responses accommodate LTE/4G/5G wireless bands. Further, the radiation plots (measurement setup) for both operating modes measured in an anechoic chamber are shown in Figure 16.

For C-mode and L-mode, centered at 2.45 and 4.0 GHz, respectively, the radiation plots for $\phi = 0°$ and $\phi = 90°$ are shown in Figure 17.
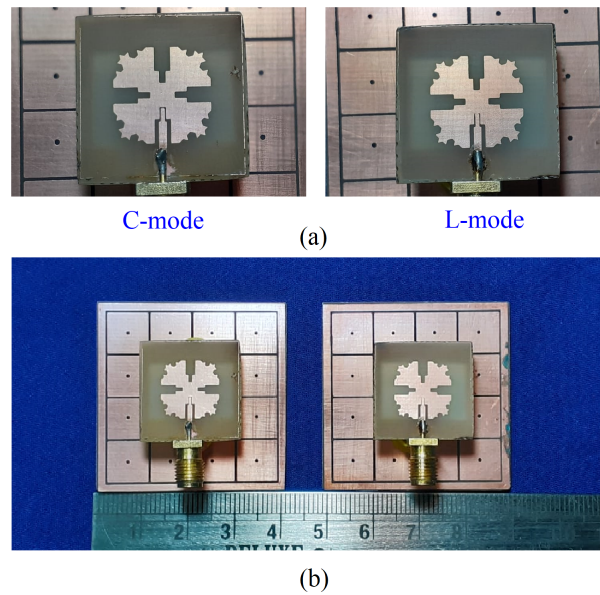

C-mode   L-mode

(a)

(b)

Figure 14. Fabricated antenna prototypes: (**a**) C-mode, L-mode (PCB printed top radiating layers) and (**b**) antennas with loaded dual AMC-MS layers.
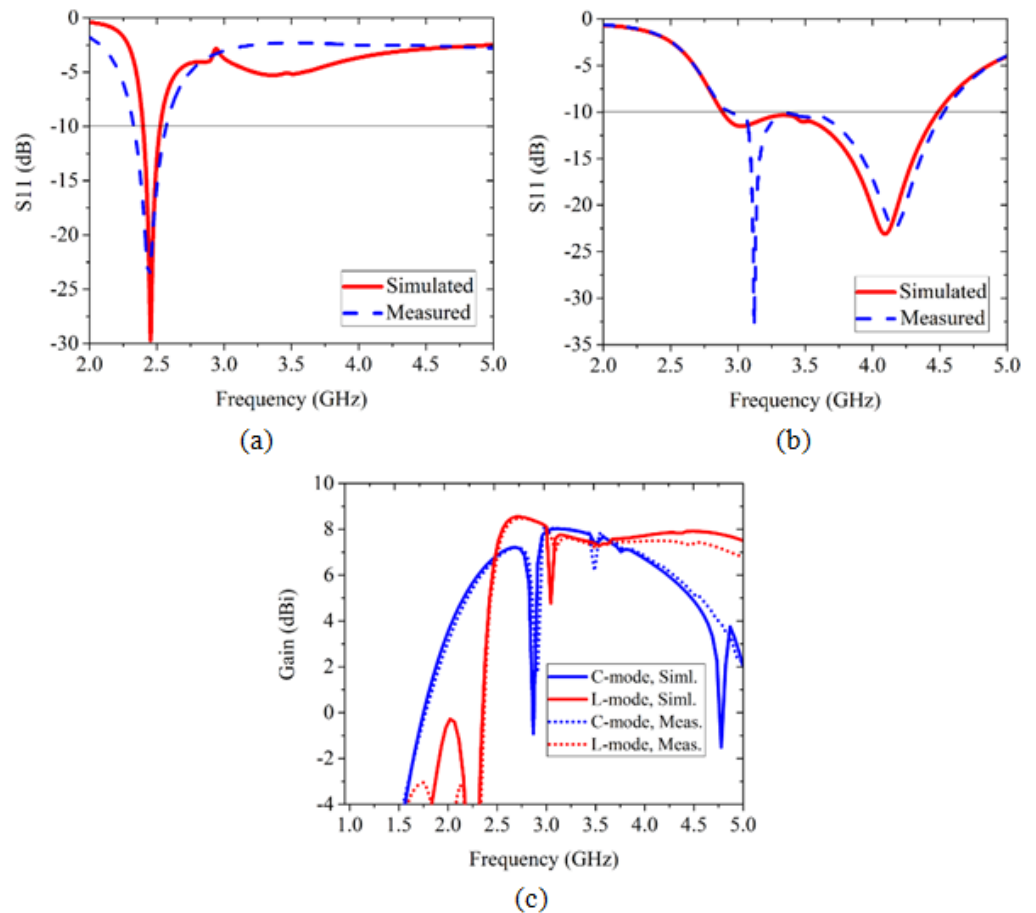

Figure 15. Simulated and measured S-parameters (S11, dB): (**a**) C-mode, (**b**) L-mode, and (**c**) Gain, dBi in both operating modes at their desired operating bands.
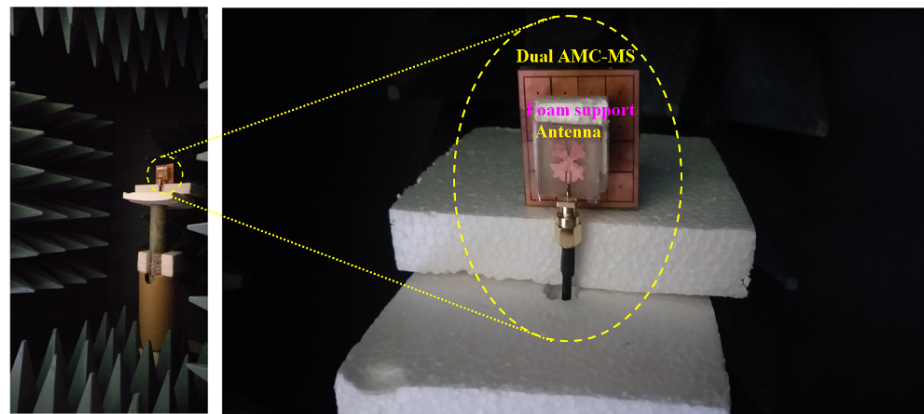
Figure 16. Far-field measurement setup of proposed antenna configuration inside anechoic chamber.
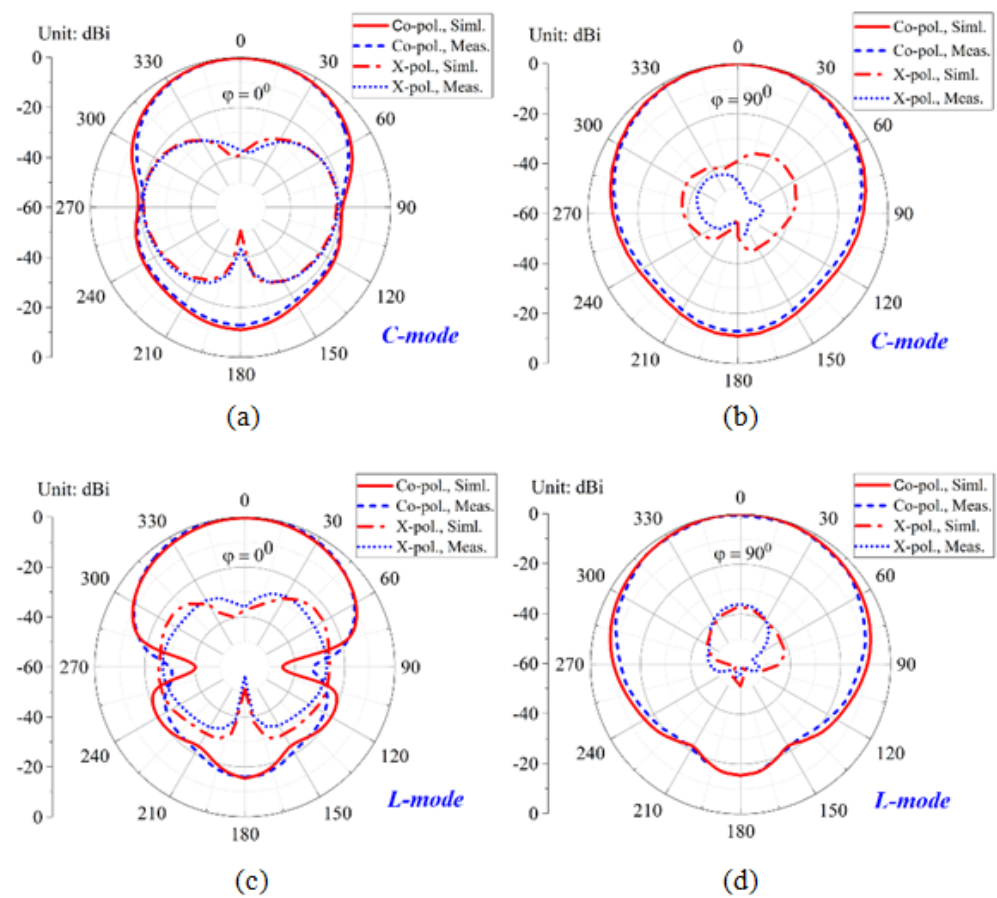

Figure 17. Simulated and measured radiation plots of the proposed antenna configuration at (**a**) 2.45 GHz ($\phi = 0°$), (**b**) 2.45 GHz ($\phi = 90°$), (**c**) 4.0 GHz ($\phi = 0°$), and (**d**) 4.0 GHz ($\phi = 90°$).

At $\phi = 0°$, we can witness a di-pole-like broad pattern, and for $\phi = 90°$, an omnidirectional pattern. Due to a low x-pol. component, the normalized magnitude of farfield strength is plotted from 0 to -60 dBi, toward getting clarity of co-pol. and x-pol. discrimination. Owing to the AMC-MS reflector layers, it possesses stable FBR at both radiation planes ranging from -15 to -17.5 dBi. The boresight radiation has maximum intensity at $\theta = 0°$ ($+ z$-axis). It is to be noted that, due to the ground aperture, the effect of capacitance plays a vital role in the reduction of x-pol. magnitudes. For $\phi = 0°$, x-pol. has < -35 dB and < -40 dB for $\phi = 90°$, respectively.

The simulated gain for C-mode was 6.74 dBi at 2.45 GHz, and the measured gain was 6.68 dBi. Similarly, L-mode gain was 7.7 dBi at 4.0 GHz, and the measured gain was

7.5 dBi. For both modes, the antenna had a peak gain variation of 8–8.6 dBi. The gain with AMC-MS layers has been compared with that from PEC reflectors for both modes, as shown in Figure 18a,b. It can be observed that the AMC-MS has superior performance compared to conventional PEC reflectors. This shows that AMC-MS has better reflection properties due to the presence of a coupling effect of inductance ($L_a + L_u + L_h$) and capacitance C_a, which controls the gap fringing fields to be effectively coupled with the antenna radiation fields. The simulated and measured efficiency plots are presented in Figure 19a,b. The simulated peak efficiency at 2.45 GHz was 81% and the measured peak efficiency was 78% for C-mode. For L-mode, the simulated peak efficiency at 4.0 GHz was 95%, and the measured peak efficiency was 92%. The average efficiency of the proposed antenna at two operating modes was >70%. The proposed printed antenna is supported by the AMC-MS via craft foam sheets. External unavoidable factors, such as substrate dielectric effects, reflector layers, and SMA losses, cause discrepancies between simulated and measured results. The notching effect in gain and efficiency can be observed, due to the geometrical configuration of the bow-tie slot structure of the radiator [27–29].
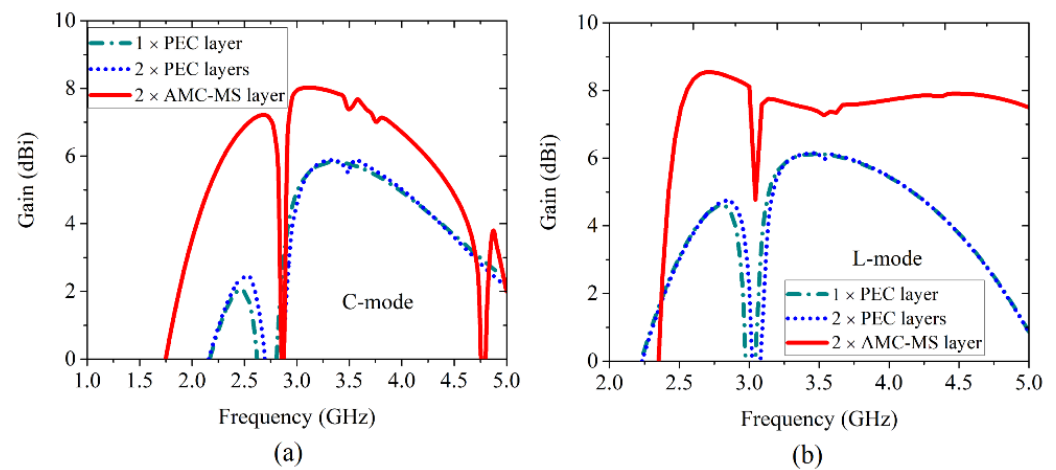

Figure 18. Comparison of simulated gain plots of the proposed antenna configuration: (**a**) C-mode and (**b**) L-mode, using PEC and AMC-MS reflectors.
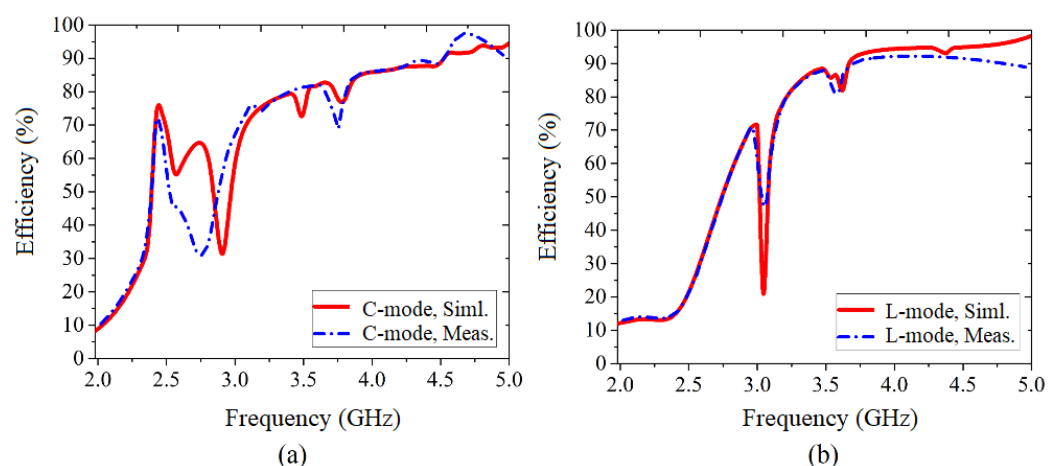

Figure 19. The simulated and measured antenna efficiency plots of the proposed antenna configuration: (**a**) C-mode and (**b**) L-mode.

Table 4 depicts the performance comparison analysis of different MS antenna parameters with the proposed antenna configuration. It can be observed that for the proposed antenna, which leverages a compact design with a reduced electrical footprint for the antenna and a reduced size of the reflector, stable performances occurred in high antenna gain and directional radiation patterns in both operating modes.

5. Key Design Aspects of the Proposed Antenna Configuration

- In the proposed design, the antenna size is half the size of the reflector. The reflector size is almost 60% reduced as compared to the conventional AMC-MS reflector. Due to the reduction in its size, the AMC's effective height is fixed at $H_{eff}/\lambda_\circ = 0.22$, for better impedance matching and stable boresight radiations. Hence, performance metrics, along with compact antenna design, are satisfied from the wireless application perspective [30].

Table 4. The performance comparison of proposed antenna configuration over the reported antenna designs in [4–14].

Ref.	Antenna Footprint ($\lambda_\circ^2$)	$f_\circ$ (GHz)	Impedance Bandwidth (%)	Gain (dBi)	Antenna Height ($\lambda_\circ$)	Circuit Analysis
[4]	0.062	1.9, 2.5	5.8, 4	4.52, 4.15	0.045	×
[5]	1.11	2.6, 3.5	7.7, 5.71	7.82, 8.6	0.09	×
[6]	1.211	(3.2–3.65)	13.13	(6.8–7.2)	0.324	×
[7]	0.54	(0.69–0.96)	32.72	(7.4–9.2)	0.1	×
[8]	0.225	2.3	34	(4.7–5.9)	0.23	×
[9]	0.75	(3–4.1)	31	7.1	0.15	×
[10]	1.5	(1.7–2.7)	45	6.3	0.25	×
[11]	0.0135	(2.8–3.2)	13.33	4	0.007	×
[12]	0.12	(1.19–2.37)	66.3	6	0.12	×
[13]	1.63	(2.47–2.77)	11.63	9.7	0.101	×
[14]	0.112	(1.647–1.94)	16.7	6.5	0.124	×
C-mode (Prop.)	0.00256	(2.33–2.574)	9.8	6.74	0.22	YES
L-mode (Prop.)	0.00256	(2.91–4.53)	43.54	7.7	0.22	YES

Notation used—$f_\circ$: operating frequency, $\lambda_\circ$: free-space wavelength at lowest operating frequency of corresponding antenna configuration.

- The inherent bow-tie-shaped fractal radiator reduces the electrical footprint by antenna size. It is difficult to excite such a compact antenna with the dual-loaded AMC reflectors; hence, tuning of the feeding mechanism has been performed, which transduces excitation energy by two induced coupling modes [31]. Thus, the feeding mechanism generates dual-mode coupling, due to induced resonance, for which dual-polarized behavior was observed.
- The dual-loaded AMC-MS reflector also initiates an effective coupling process, and the ground aperture emulsifies the coupled energy into the boresight radiation; hence, there are no spurious NULLS. The dual reflectors also increase the radiation strength, the boresight gain is enhanced, and the back lobe radiation is reduced [32,33].
- The aperture in the ground plane of the antenna is a defected ground element aiming at the reduction of x-pol. in the both radiated planes. Since the design is very compact, co-pol. radiation stability and its high differentiation from the x-pol. are also taken into consideration [34–36], primarily focusing towards the wireless applications point-of-view [37–47].
- Since the design objective was compactness, the mutual inductance effects of dual-loaded AMC-MS layers were stabilized, and optimized antenna performance was obtained due to the low-profile effective height consideration.
- The compact low-profile antenna design with a premium footprint satisfied design metrics; and impedance performances, antenna gain, and radiation efficiency satisfied

performance metrics in our proposed design implementation with reference to the designs reported in [29,40].

- The initial attempt at a reconfigurable approach in the feeding mechanism has some limitations—i.e., when a diode is placed in the adjoining point of contact between radiator and feed, due to the dominant effect of inductance, as the course of frequency shifting is invariant. Thus, an independent feeding mechanism has been adopted and reported in this proposed work.

6. Conclusions

In this research article, a dual-mode-induced, dual-polarized, compact, directional, bow-tie-shaped fractal patch antenna was realized. It has dual metasurface layers with high gain for LTE/4G/5G wireless applications. The induced coupling modes have two different operating frequency bands: 2.33–2.57 GHz with a bandwidth of 0.24 GHz as C-mode and from 2.91 to 4.53 GHz with a bandwidth of 1.62 GHz as L-mode. The aperture in the ground copulates reflection waves from dual AMC-MS to radiate in the boresight direction, reducing the x-pol component with the attainment of a stable front-to-back ratio (FBR). The gain and efficiency at the two working modes are 6.68 dBi (78%) and 7.5 dBi (92%) in their respective operating bands.

References

1.　Wang, J.; Li, Y.; Jiang, Z.H.; Shi, T.; Tang, M.C.; Zhou, Z.; Qiu, C.W. Metantenna: When Metasurface Meets Antenna Again. *IEEE Trans. Antennas Propag.* **2020**, *68*, 1332–1347. [CrossRef]
2.　Decoster, B.; Maes, S.; Cuiñas, I.; García Sánchez, M.; Caldeirinha, R.; Verhaevert, J. Dual-band single-layer fractal frequency selective surface for 5G applications. *Electronics* **2021**, *10*, 2880. [CrossRef]
3.　Al-Gburi, A.J.A.; Ibrahim, I.M.; Zakaria, Z.; Abdulhameed, M.K.; Saeidi, T. Enhancing gain for UWB antennas using FSS: A systematic review. *Mathematics* **2021**, *9*, 3301. [CrossRef]
4.　Yue, T.; Jiang, Z.H.; Panaretos, A.H.; Werner, D.H. A compact dual-band antenna enabled by a complementary split-ring resonator-loaded metasurface. *IEEE Trans. Antennas Propag.* **2017**, *65*, 6878–6888. [CrossRef]
5.　Liu, F.; Guo, J.; Zhao, L.; Huang, G.L.; Li, Y.; Yin, Y. Dual-band metasurface-based decoupling method for two closely packed dual-band antennas. *IEEE Trans. Antennas Propag.* **2019**, *68*, 552–557. [CrossRef]
6.　Guo, J.; Liu, F.; Zhao, L.; Yin, Y.; Huang, G.L.; Li, Y. Meta-surface antenna array decoupling designs for two linear polarized antennas coupled in H-plane and E-plane. *IEEE Access* **2019**, *7*, 100442–100452. [CrossRef]
7.　Zhu, H.; Qiu, Y.; Wei, G. A broadband dual-polarized antenna with low profile using nonuniform metasurface. *IEEE Antennas Wirel. Propag. Lett.* **2019**, *18*, 1134–1138. [CrossRef]
8.　Martinis, M.; Bernard, L.; Mahdjoubi, K.; Sauleau, R.; Collardey, S. Wideband antenna in cavity based on metasurfaces. *IEEE Antennas Wirel. Propag. Lett.* **2015**, *15*, 1053–1056.
9.　Zhu, J.; Li, S.; Liao, S.; Xue, Q. Wideband low-profile highly isolated MIMO antenna with artificial magnetic conductor. *IEEE Antennas Wirel. Propag. Lett.* **2018**, *17*, 458–462. [CrossRef]
10.　Wu, J.; Yang, S.; Chen, Y.; Qu, S.; Nie, A. A low profile dual-polarized wideband omnidirectional antenna based on AMC reflector. *IEEE Trans. Antennas Propag.* **2016**, *65*, 368–374. [CrossRef]

11. Jafargholi, A.; Jafargholi, A. Miniaturisation of printed slot antennas using artificial magnetic conductors. *IET Microw. Antennas Propag.* **2018**, *12*, 1054–1059. [CrossRef]

12. Feng, D.; Zhai, H.; Xi, L.; Yang, S.; Zhang, K.; Yang, D. A broadband low-profile circular-polarized antenna on an AMC reflector. *IEEE Antennas Wirel. Propag. Lett.* **2017**, *16*, 2840–2843. [CrossRef]

13. Yang, F.H.; Tang, W. A novel low-profile high-gain antenna based on artificial magnetic conductor for LTE applications. In Proceedings of the IEEE ISAPE2012, Xi'an, China, 22–26 October 2012; pp. 171–174.

14. Zhong, Y.W.; Yang, G.M.; Zhong, L.R. Gain enhancement of bowtie antenna using fractal wideband artificial magnetic conductor ground. *Electron. Lett.* **2015**, *51*, 315–317. [CrossRef]

15. Ameen, M.; Chaudhary, R.K. Metamaterial circularly polarized antennas: Integrating an epsilon negative transmission line and single split ringtype resonator. *IEEE Antennas Propag. Mag.* **2021**, *63*, 60–77. [CrossRef]

16. Ameen, M.; Chaudhary, R.K. Metamaterial-based wideband circularly polarised antenna with rotated V-shaped metasurface for small satellite applications. *Electron. Lett.* **2019**, *55*, 365–366. [CrossRef]

17. Agarwal, K.; Nasimuddin; Alphones, A. Wideband circularly polarized AMC reflector backed aperture antenna. *IEEE Trans. Antennas Propag.* **2012**, *61*, 1456–1461. [CrossRef]

18. Feng, B.; Lai, J.; Zeng, Q.; Chung, K.L. A dual-wideband and high gain magneto-electric dipole antenna and its 3D MIMO system with metasurface for 5G/WiMAX/WLAN/X-Band applications. *IEEE Access* **2018**, *6*, 33387–33398. [CrossRef]

19. Wang, J.; Wong, H.; Ji, Z.; Wu, Y. Broadband CPW-fed aperture coupled metasurface antenna. *IEEE Antennas Wirel. Propag. Lett.* **2019**, *18*, 517–520. [CrossRef]

20. Juan, Y.; Yang, W.; Che, W. Miniaturized low-profile circularly polarized metasurface antenna using capacitive loading. *IEEE Trans. Antennas Propag.* **2019**, *67*, 3527–3532. [CrossRef]

21. Agarwal, K.; Nasimuddin; Alphones, A. Unidirectional wideband circularly polarised aperture antennas backed with artificial magnetic conductor reflectors. *IET Microw. Antennas Propag.* **2013**, *7*, 338–346. [CrossRef]

22. Yang, S.; Chen, Y.; Yu, C.; Gong, Y.; Tong, F. Design of a low-profile, frequency-reconfigurable, and high gain antenna using a varactor-loaded AMC ground. *IEEE Access* **2020**, *8*, 158635–158646. [CrossRef]

23. Raad, H.R.; Abbosh, A.I.; Al-Rizzo, H.M.; Rucker, D.G. Flexible and compact AMC based antenna for telemedicine applications. *IEEE Trans. Antennas Propag.* **2012**, *61*, 524–531. [CrossRef]

24. Majumder, B.; Krishnamoorthy, K.; Mukherjee, J.; Ray, K.P. Compact broadband directive slot antenna loaded with cavities and single and double layers of metasurfaces. *IEEE Trans. Antennas Propag.* **2016**, *64*, 4595–4606. [CrossRef]

25. Nasimuddin, N.; Chen, Z.N.; Qing, X. Bandwidth enhancement of a single-feed circularly polarized antenna using a metasurface: Metamaterial-based wideband CP rectangular microstrip antenna. *IEEE Antennas Propag. Mag.* **2016**, *58*, 39–46. [CrossRef]

26. Nie, N.S.; Yang, X.S.; Chen, Z.N.; Wang, B.Z. A low-profile wideband hybrid metasurface antenna array for 5G and WiFi systems. *IEEE Trans. Antennas Propag.* **2019**, *68*, 665–671. [CrossRef]

27. Behera, B.R. Sierpinski Bow-Tie antenna with genetic algorithm. *Eng. Sci. Technol. Int. J.* **2017**, *20*, 775–782. [CrossRef]

28. Gonçalves Licursi de Mello, R.; Lepage, A.C.; Begaud, X. The bow-tie antenna: Performance limitations and improvements. *IET Microw. Antennas Propag.* **2022**, *16*, 283–294. [CrossRef]

29. Faouri, Y.S.; Ahmad, S.; Parchin, N.O.; See, C.H.; Abd-Alhameed, R. A novel meander bowtie-shaped antenna with multi-resonant and rejection bands for modern 5G communications. *Electronics* **2022**, *11*, 821. [CrossRef]

30. Baba, A.A.; Hashmi, R.M.; Esselle, K.P. Achieving a large gain bandwidth product from a compact antenna. *IEEE Trans. Antennas Propag.* **2017**, *65*, 3437–3446. [CrossRef]

31. Liu, J.; Zhong, S.; Esselle, K.P. A printed elliptical monopole antenna with modified feeding structure for bandwidth enhancement. *IEEE Trans. Antennas Propag.* **2010**, *59*, 667–670. [CrossRef]

32. Premathilake, T.; Jayasinghe, J.; Saraereh, O.; Esselle, K.; Khokle, R. High directivity broadband hexagonal fractal ring antenna with modified ground. *ECTI Trans. Electr. Eng. Electron. Commun.* **2020**, *18*, 1–8. [CrossRef]

33. Li, M.; Li, Q.L.; Wang, B.; Zhou, C.F.; Cheung, S.W. A low-profile dual-polarized dipole antenna using wideband AMC reflector. *IEEE Trans. Antennas Propag.* **2018**, *66*, 2610–2615. [CrossRef]

34. Liu, W.; Chen, Z.N.; Qing, X. Metamaterial-based low-profile broadband aperture-coupled grid-slotted patch antenna. *IEEE Trans. Antennas Propag.* **2015**, *63*, 3325–3329. [CrossRef]

35. Mohanty, A.; Behera, B.R.; Nasimuddin, N. Hybrid metasurface loaded tri-port compact antenna with gain enhancement and pattern diversity. *Int. J. RF Microw. Comput. Eng.* **2021**, *31*, e22795. [CrossRef]

36. Sahu, N.K.; Mishra, S.K. Compact dual-band dual-polarized monopole antennas using via-free metasurfaces for off body communications. *IEEE Antennas Wirel. Propag. Lett.* **2022**. *early access*. [CrossRef]

37. Li, J.; Huo, H.; Chen, J.; Zhu, S.; Shi, H.; Zhang, A. Miniaturised artificial magnetic conductor and its application in unidirectional circularly polarised slot antenna design. *IET Microw. Antennas Propag.* **2018**, *55*, 1885–1889. [CrossRef]

38. Burokur, S.N.; Germain, D.; Ratajczak, P.; Daniel, J.P.; De Lustrac, A. GSM/DCS/UMTS low-profile metamaterial-based microwave antenna. *Microw. Opt. Technol. Lett.* **2015**, *57*, 737–741. [CrossRef]

39. Hongyu, S.; Zhu, S.; Li, J.; Zhang, A.; Xu, Z. Cross-polarization suppression in C-shaped microstrip patch antenna employing anisotropic dielectrics. *J. Adv. Dielectr.* **2017**, *7*, 1.

40. Nasimuddin; Esselle, K.P. A low-profile compact microwave antenna with high gain and wide bandwidth. *IEEE Trans. Antennas Propag.* **2007**, *55*, 1880–1883.

41. Vaidya, A.R.; Gupta, R.K.; Mishra, S.K.; Mukherjee, J. High-gain low side lobe level fabry perot cavity antenna with feed patch array. *Prog. Electromagn. Res. C* **2012**, *28*, 223–238. [CrossRef]

42. Vaidya, A.R.; Gupta, R.K.; Mishra, S.K.; Mukherjee, J. Right-hand/left-hand circularly polarized high-gain antennas using partially reflective surfaces. *IEEE Antennas Wirel. Propag. Lett.* **2014**, *13*, 431–434. [CrossRef]

43. Behera, B.R.; Srikanth, P.; Meher, P.R.; Mishra, S.K. A compact broadband circularly polarized printed monopole antenna using twin parasitic conducting strips and rectangular metasurface for RF energy harvesting application. *AEU-Int. J. Electron. Commun.* **2020**, *120*, 153233. [CrossRef]

44. Behera, B.R.; Meher, P.R.; Mishra, S.K. Metasurface superstrate inspired printed monopole antenna for RF energy harvesting application. *Prog. Electromagn. Res. C* **2021**, *110*, 119–133. [CrossRef]

45. Behera, B.R.; Mohanty, A. Dual-polarized metasurface-based monopole antenna design using characteristics mode theory for UHF RFID applications. *Int. J. Microw. Comput.-Aided Eng.* **2022**, e23325. *early access*. [CrossRef]

46. Alsharif, M.H.; Nordin, R. Evolution towards fifth generation (5G) wireless networks: Current trends and challenges in the deployment of millimetre wave, massive MIMO, and small cells. *Telecommun. Syst.* **2017**, *64*, 617–637. [CrossRef]

47. Alsharif, M.H.; Kelechi, A.H.; Albreem, M.A.; Chaudhry, S.A.; Zia, M.S.; Kim, S. Sixth generation (6G) wireless networks: Vision, research activities, challenges and potential solutions. *Symmetry* **2020**, *12*, 676. [CrossRef]